ACS NANO

www.acsnano.org

ARTICLE

Desalination and Nanofiltration through Functionalized Laminar MoS_2 Membranes

Wisit Hirunpinyopas,[†,‡,§] Eric Prestat,[‡] Stephen D. Worrall,[§,∥] Sarah J. Haigh,[‡] Robert A. W. Dryfe,[*,†,§] and Mark A. Bissett[*,†,‡]

[†]National Graphene Institute, [‡]School of Materials, and [§]School of Chemistry, University of Manchester, Oxford Road, Manchester M13 9PL, United Kingdom

Supporting Information

ABSTRACT: Laminar membranes of two-dimensional materials are excellent candidates for applications in water filtration due to the formation of nanocapillaries between individual crystals that can exhibit a molecular and ionic sieving effect, while allowing high water flux. This approach has been exemplified previously with graphene oxide, however these membranes suffer from swelling when exposed to liquid water, leading to low salt rejection and reducing their applicability for desalination applications. Here, we demonstrate that by producing thin (~5 μm) laminar membranes of exfoliated molybdenum disulfide (MoS_2) in a straightforward and scalable process, followed by a simple chemical functionalization step, we can efficiently reject ~99% of the ions commonly found in seawater, while maintaining water fluxes significantly higher (~5 times) than those reported for graphene oxide membranes. These functionalized MoS_2 membranes exhibit excellent long-term stability with no swelling and consequent decrease in ion rejection, when immersed in water for periods exceeding 6 months. Similar stability is observed when exposed to organic solvents, indicating that they are ideal for a variety of technologically important filtration applications.

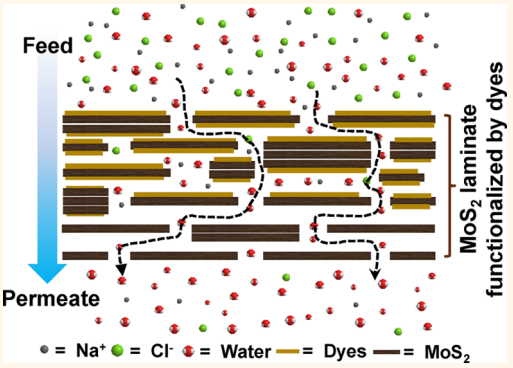

KEYWORDS: *MoS_2, filtration, desalination, membrane, functionalization, nanomaterials*

Environmental pressures, along with the discovery of two-dimensional (2D) materials such as graphene, have combined to provide renewed interest in the development of membrane technologies.[1,2] Membrane technology is favored over other purification techniques such as disinfection or distillation due to the lack of chemical additives, energy efficiency, and simplicity of the technology. Most of the commercial filtration membranes that are currently available are composed of polymeric materials including polysulfone and polyamides, however a variety of mesoporous ceramic and zeolite-based materials have also been investigated.[2] Polymeric membranes are hindered by the lack of high temperature stability, combined with low resistance to strongly acidic/alkaline environments and organic solvents, while ceramics remain expensive for large-scale applications and zeolite membranes are hindered by their low water flux.

2D materials, as exemplified originally by graphene and graphene oxide (GO), present a different approach to filtration by forming a layered structure consisting of nanocapillary channels. These laminar membranes provide versatility as the solute rejection and solvent transport properties can be tuned by altering the preparation methods or surface functionality[3−5] and have demonstrated much higher water flux than those of polymeric membranes,[5,6] while also demonstrating ionic selectivity.[7,8] GO-based membranes are, however, prone to swelling when exposed to liquid water and suffer from poor long-term stability.[9] The resultant increase in interlayer separation means these membranes display low rejection of the ions commonly found in seawater, preventing their widespread use.[5,7] It has been recently demonstrated that physically restricting these GO-based membranes reduces this swelling and achieves higher ionic rejection, however, only at the cost of poorer water permeation rates, and this process necessitates a difficult to scale polymer encapsulation procedure.[10] Consequently, the rejection properties exhibited by previously reported examples of graphene and GO membranes are far from that needed for widespread adoption of 2D material-based desalination membranes.[5,11,12]

Recent work has suggested that other 2D layered materials, such as the transition-metal dichalcogenides (TMDs), could be suitable for applications in water filtration.[13−15] Despite this, there have been few reported studies of the filtration properties of these TMD materials. The existing reports for MoS_2- and WS_2-based membranes demonstrate excellent improvements in water flux, up to 2−5 times greater than GO-based membranes

Received: July 20, 2017
Accepted: October 11, 2017
Published: October 11, 2017

DOI: 10.1021/acsnano.7b05124
ACS Nano 2017, 11, 11082−11090

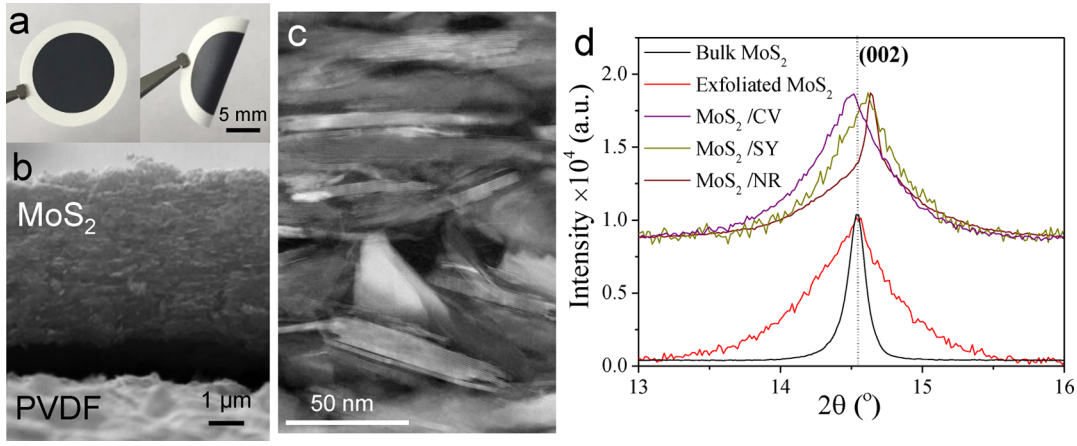

Figure 1. (a) Photograph of the MoS_2 membrane supported by a polymer (PVDF) demonstrating their flexibility. (b) Cross-sectional SEM image of the formed MoS_2 membrane supported on the PVDF showing the stacked layered nature of the MoS_2. Membranes were produced with thicknesses varying from 1 to 10 μm. (c) Low-angle annular dark-field (LAADF) STEM image showing the cross-section of a laminate MoS_2 membrane. The thickness of individual flakes is ~1−10 layers, with the majority being few-layers (3−5). (d) PXRD pattern of the (002) peak position for each of the functionalized membranes, pristine exfoliated MoS_2, and the bulk starting material.

of comparable thickness.[16,17] These TMD membranes also show promising rejection (>80%) of large (~1 nm) organic molecules, but their ionic rejection properties remain largely unexplored[18] and require further investigation to understand the behavior of the nanocapillary channels formed between the TMD layers. There have been promising theoretical investigations into the performance of individual pores in MoS_2 layers which suggest that defect sites, with exposed Mo atoms, yield water permeation rates 2−5 orders of magnitude greater than commercially available materials.[19]

In this work, we show that ion-selective filtration membranes can be fabricated from laminar films of MoS_2 and demonstrate that these MoS_2 membranes exhibit excellent ionic sieving for all major cationic components commonly found in seawater (*e.g.*, Na^+, K^+, Ca^{2+}, and Mg^{2+}), while still possessing high water permeation rates. Significantly, we demonstrate that chemical functionalization is necessary to impart the desired ionic sieving properties by altering the surface charge present on the MoS_2 membrane. These chemically functionalized MoS_2 membranes exhibit superior long-term stability with no change in the ionic rejection properties even after being continuously immersed in liquid water for over 6 months. Furthermore, the MoS_2 membranes were found to be tolerant to solvent exposure in general, with immersion in solvents of varying polarity having no appreciable effect on the interlayer spacing (Figure S1), unlike GO membranes which suffer from various degrees of swelling.[20] This demonstrates that these membranes are suitable not only for water filtration but also have potential in a variety of nonaqueous filtration applications.[20−22] This stability of the MoS_2 membranes is in agreement with a recent study which found them to be highly stable in aqueous environments, even with varying pH.[18]

RESULTS AND DISCUSSION

Producing Laminar MoS_2 Membranes. MoS_2 membranes were produced by filtration of solvent stabilized dispersions of exfoliated MoS_2 flakes, where different volumes were filtered through polyvinylidene difluoride (PVDF) supporting membranes (100 nm pores) to produce supported MoS_2 membranes of the desired thickness. The exfoliated MoS_2 flake dimensions within the dispersion (concentration ~0.02 mg mL^{-1} in 1:1 isopropanol/water mixtures) were characterized and found to have thicknesses in the several (1−5) layer range and lateral dimensions of 200−300 nm, as determined by electron microscopy and Raman spectroscopy. The PVDF supporting membranes alone were also characterized and found to exhibit no ionic selectivity or separation ability toward simple salts and thus do not affect the MoS_2 membrane performance. Figure 1a shows a photograph of one of the MoS_2 membranes supported on a PVDF filter, also illustrating their flexibility. Figure 1b shows a low-magnification cross-sectional scanning electron microscope (SEM) image which shows the laminar structure of the MoS_2 sheets. For this work, membranes of various thicknesses between 1 and 10 μm were produced as specified (Figure S2).

The MoS_2 membranes were functionalized by immersion in different dye solutions for extended periods (~21 days), in order to tune their permeation properties, as shown in Figure S3. The dye molecules investigated were a cationic dye commonly known as crystal violet (CV) (tris(4-(dimethylamino)phenyl)methylium chloride), an anionic dye known as sunset yellow (SY) (disodium 6-hydroxy-5-[(4-sulfophenyl)azo]-2-naphthalenesulfonate), and an uncharged dye called neutral red (NR) (3-amino-7-dimethylamino-2-methylphenazine). Dye-functionalized membranes are referred to as MoS_2/CV, MoS_2/SY, and MoS_2/NR. The laminar structure of the stacked MoS_2 sheets within the as-prepared membranes can be observed directly from the scanning transmission electron microscope (STEM) image shown in Figure 1c, where the individual nanosheets of horizontally stacked MoS_2 can be seen, in addition to several out-of-plane sheets. The powder X-ray diffraction (PXRD) patterns comparing the (002) peak of the pristine and functionalized MoS_2 membranes (with PVDF supports) are shown in Figure 1d. It is clearly seen that the (002) peak after exfoliation is significantly broader compared to the starting material, indicating a distribution in flake size as the ultrasonication process reduces the lateral size from several microns to a few hundred nm. The PXRD patterns of the dye-functionalized MoS_2 membranes immersed in water >6 months are also shown in Figure 1d. The functionalized MoS_2 membranes show little change (~0.04 Å) in peak position, indicating that the

DOI: 10.1021/acsnano.7b05124
ACS Nano 2017, 11, 11082−11090

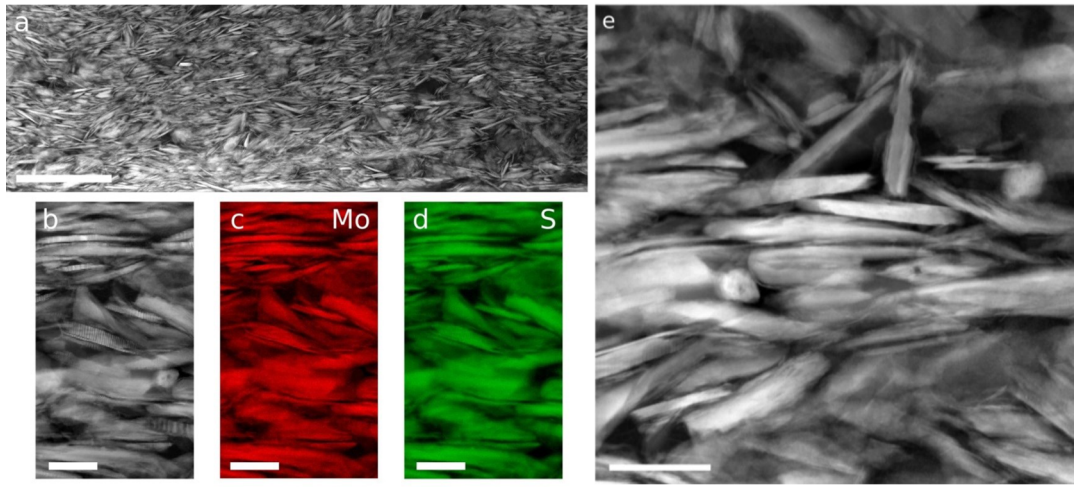

Figure 2. Cross-sectional STEM imaging of a functionalized MoS_2/CV membrane showing the distribution and orientation of MoS_2 flakes in the membranes. (a) Overview HAADF-STEM image of the membrane, the scale bar in (a) is 500 nm. (b–d) HAADF image, Mo and S EELS maps, and (e) high-resolution HAADF-STEM image of the membrane. The scale bars in b–e are 50 nm.

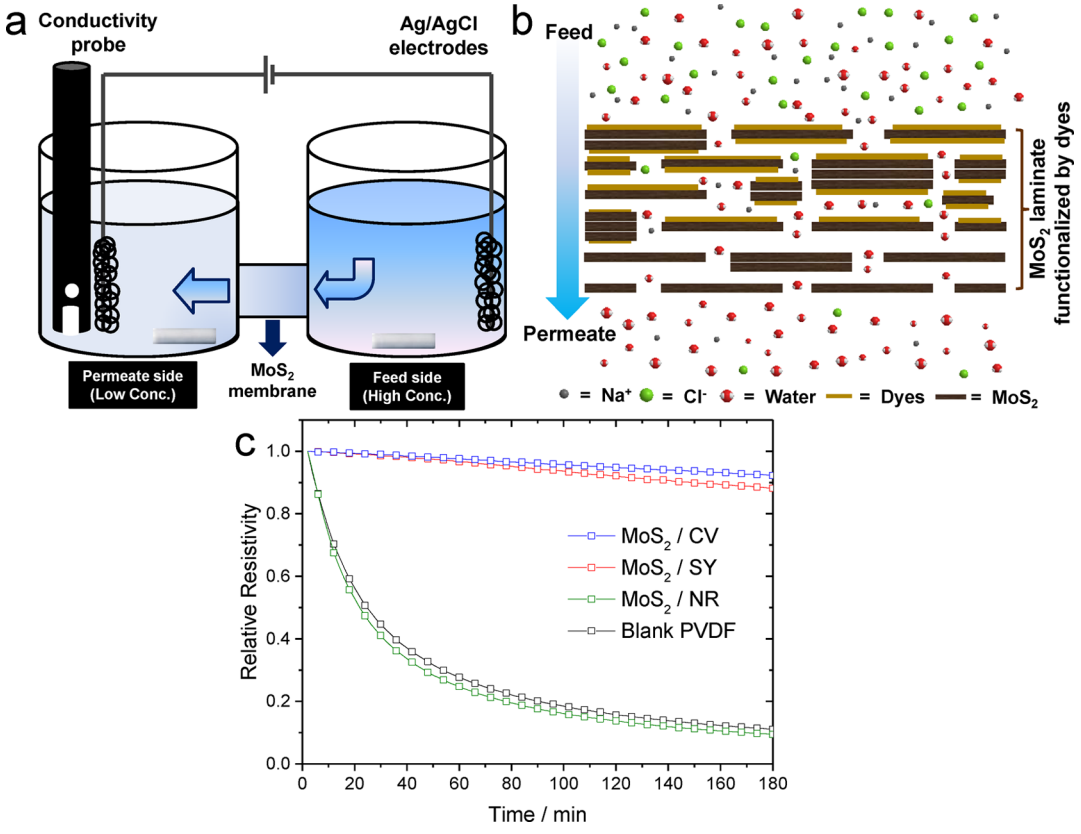

Figure 3. (a) Schematic of the experimental setup used for the ionic permeation experiments. (b) Schematic showing the diffusion, driven by the large concentration gradient, of the solute (Na^+ and Cl^- ions in this case) through the MoS_2 laminate membrane which has been prefunctionalized by organic dye. (c) Plot comparing the change in relative resistivity of the permeate side of 6 μm-thick MoS_2 laminate membranes functionalized with different dyes SY, CV, and NR and for the bare PVDF filter, when the feed side initially contains 1 M NaCl and the permeate side is 1000 times more dilute (1 mM).

membrane did not undergo any significant swelling in liquid water with prolonged exposure.

Further analysis of the cross-sectional STEM images was performed to gain insight in the morphology and the stacking of the MoS_2 flakes within the membrane. Figure 2 shows the STEM data for a functionalized (MoS_2/CV) membrane. In Figure 2 an overview (Figure 2a), the Mo and S elemental maps (Figure 2c–d) obtained using STEM-EELS and a high resolution HAADF-STEM (Figure 2e) are shown. The thickness of the flakes ranges from monolayers to 15 layers, with most the flakes being 3–5 layers thick. The overview images and the Mo and S elemental maps confirm that the MoS_2 flakes are homogeneous across the whole membrane. Figure 2e highlights the fact that all the flakes are not stacked

DOI: 10.1021/acsnano.7b05124
ACS Nano 2017, 11, 11082–11090

along the same direction, for example, in the plane of the membrane, as could be initially anticipated; this was also supported by analysis of the Fourier transforms of lattice resolution HAADF STEM images which were used to determine flake orientation (Figure S5). This apparent disorder within the membrane may be a result of the smaller flake size, compared to GO membranes which typically consist of flakes on the order of >1 μm diameter.[4,5] The relatively small MoS_2 flakes are able to produce a membrane with very high surface area and a large amount of exposed edges, leading to the formation of a large number of nanocapillaries throughout the membrane.

Water Permeation Rates. Water permeation rates through the MoS_2 membranes were calculated using two different methods to allow for a direct comparison of relative performance: First, the osmotic pressure method demonstrated for GO membranes by Joshi *et al.*,[7] where an aqueous sucrose solution (1 M) is placed on one side of the membrane and distilled water on the other. By measuring the change in volume of the water on the feed side, we can approximate the permeation rate. This was found to be 40×10^{-3} L m^{-2} h^{-1} bar^{-1} for a 3 μm-thick membrane and 11.6×10^{-3} L m^{-2} h^{-1} bar^{-1} for a 6 μm-thick membrane (both functionalized by CV dye). This demonstrates the significant improvement over the GO membranes studied previously which exhibited a permeation of $\sim 8 \times 10^{-3}$ L m^{-2} h^{-1} bar^{-1} for a 1 μm-thick membrane,[7] demonstrating the increased water flux possible through MoS_2 membranes. This also agrees with previous literature reports which demonstrated water permeation rates 3−5 times higher for MoS_2 membranes compared to GO[17] and also compares favorably to MoS_2 membranes produced through chemical exfoliation which showed permeation rates measured by osmotic pressure (1 M NaCl) of 2.2×10^{-3} L m^{-2} h^{-1} bar^{-1}.[18]

Second, external pressure was used in a dead-end filtration setup to calculate the water permeation rate. The water permeation rate under external pressure was found to be 269.5 (±23.7) L m^{-2} h^{-1} bar^{-1} for a 6 μm-thick MoS_2/CV membrane. This exceeds the performance of similar external pressure results for pristine MoS_2 laminates, which showed a lower permeation rate of 245 L m^{-2} h^{-1} bar^{-1} for a much thinner (1.7 μm thick) membrane.[17] The large difference in calculated water flux for the two methods, osmotic pressure and external pressure, is attributed to the inevitable presence of a concentration gradient of sucrose, which will reduce the transmembrane pressure. The water permeation rates for each membrane are summarized in Table S1. Interestingly, the water flux as a function of membrane thickness follows the standard Hagen−Poiseuille[11] model for the pristine membranes, but after dye functionalization the change in surface chemistry and surface wettability of the membranes leads to a deviation from established theory with the thicker (3 and 6 μm) MoS_2/CV membranes exhibiting higher water flux than the 1 μm-thick membrane (Figure S7).

Permeation of Ionic Solutes. Permeation of various solutes including organic dyes (CV, SY, and NR) and alkali metal/alkaline earth salts (KCl, NaCl, Na_2SO_4, $CaCl_2$, and $MgCl_2$) was measured using a bespoke H-beaker setup shown schematically in Figure 3a. The membranes were first sandwiched between two polyethylene terephthalate (PET) sheets with preformed holes to ensure that the exposed membrane area was controlled and reproducible. This sandwich was then sealed between two containers with equal volumes of water, to minimize any hydrostatic pressure, consisting of a "feed" side with a high concentration of the selected solute (1 M) and a "permeate" side with a thousand times lower concentration (1 mM) to ensure high diffusive flux, shown schematically in Figure 3b. Both sides of the cell underwent constant stirring to minimize concentration polarization effects. The rejection properties were measured using several techniques: Optical absorbance spectroscopy was used for the dyes; *in situ* electrochemical techniques (both conductivity and potentiometric measurements) were used to determine the change in concentration of the ionic species of the permeate side; and *ex situ* inductively coupled plasma optical emission spectrometry (ICP-OES) was used to independently measure the concentration of the solutes.

The as-prepared MoS_2 membranes (before dye functionalization) exhibit excellent rejection properties for each of the large (~1 nm) dye solute molecules, with very low permeation rates (CV: 5.3 μmol m^{-2} h^{-1}, SY: 0.9 μmol m^{-2} h^{-1}, NR: 12.5 μmol m^{-2} h^{-1}) for a 6 μm-thick membrane. However, the as-prepared membranes exhibited poor rejection of the group I and II metal cations listed previously. Importantly, the filtration properties of the membranes were found to be transformed by the dye functionalization. Following dye functionalization with the cationic (CV) and anionic (SY) dyes, they exhibited significantly decreased permeation rates of simple ionic solutes. To quantify the dynamic permeation of the solute ions, the change in resistivity of the permeate side of the membrane with increasing ionic concentration can be measured as a function of time. By starting with 1 mM of chosen solute, we minimize any potential decrease in resistivity arising from exposure to atmospheric gases (*e.g.*, CO_2). The plot in Figure 3c compares the ionic permeability of the CV, SY, and NR dye-functionalized MoS_2 membranes as well as the bare PVDF filter. In both the CV- and SY-functionalized MoS_2 membranes the relative resistivity has dropped by <10% after 3 h, indicating excellent low permeability for small ions. In contrast, the NR-functionalized membrane displays negligible rejection properties, similar to the bare PVDF filter. This indicates that it is the interaction between the ionic dye molecules and the MoS_2 flakes, which carry a negative surface charge, which leads to the ionic rejection behavior. This surface charge was measured using zeta (ζ) potential (Figure S8) and found to be −30 mV for pristine MoS_2, in agreement with previous literature.[17,23] After functionalization the values change to −16 mV for MoS_2/CV and −26 mV for MoS_2/SY. The reduction in ζ potential seen for the cationic dye is consistent with the positive charge of the attached molecule, and this change is responsible for the ionic permeation properties measured, combined with a size exclusion mechanism. Further results for each of the ionic species investigated for different membrane thicknesses and functionalization conditions can be seen in Figures S9−S11.

To complement the permeability measurements obtained from changes in resistivity, *in situ* potentiometric measurements were also performed, measuring the potential difference between two silver/silver chloride (Ag/AgCl) reference electrodes, placed in both the feed and permeate compartments, with no applied current (Figure S9). This technique has also been applied previously to measure the potential across a single pore within a MoS_2 sheet and has possible applications for energy generation.[24] To further validate the *in situ* electrochemical results, the increased concentration of sodium cations (Na^+) present in the permeate side after 3 h was determined by ICP-OES, and these values are shown in Figure

DOI: 10.1021/acsnano.7b05124
ACS Nano 2017, 11, 11082−11090

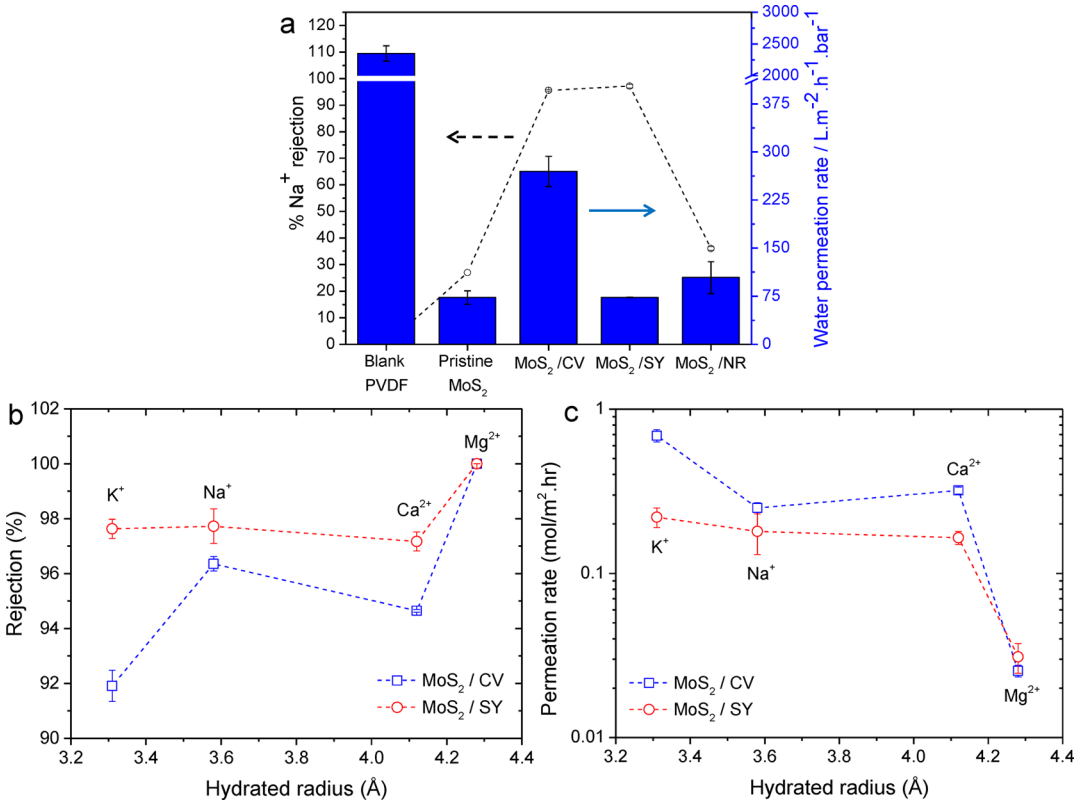

Figure 4. (a) Comparison of the sodium ion (Na^+) percentage rejection under diffusive pressure measured by ICP-OES after 180 min for each membrane (6 μm thick) as well as the water permeation rate measured with external pressure (1 bar). (b) Plot of the rejection properties ($R\% = 1 - C_{MoS2}/C_{PVDF}$) of the dye-functionalized MoS_2 membranes (6 μm thick) as a function of hydrated cation radius measured after 3 h. (c) Plot of the permeation rates for the MoS_2/CV- and MoS_2/SY-functionalized MoS_2 membranes (both 6 μm thick) for the different cationic species studied with a 1000× concentration gradient. Note the semilogarithmic scale.

4a along with the water flux determined from applied external pressure. Ionic rejection can be defined as $(1 - C_{MoS_2}/C_{PVDF})$, where C_{MoS_2} is the increased concentration of solute ions in the permeate side exposed to the diffusive pressure gradient using the dye-functionalized MoS_2 membrane, while C_{PVDF} is the increased concentration using the blank PVDF filter. The results in Figure 4a give a Na^+ rejection rate after 3 h of 96.36 (±0.27)% and 97.73 (±0.63)% for the 6 μm-thick CV- and SY-functionalized MoS_2 membranes, respectively, despite the 1000× concentration gradient. The pristine MoS_2, MoS_2/NR, and bare PVDF showed much lower rejection properties (~0–30%). These results are in excellent agreement with the resistivity results and indicate that the cationic and anionic dye-functionalized membranes, MoS_2/CV and MoS_2/SY, are able to efficiently reduce the permeability of Na^+ and Cl^- ions. Recently, Abraham *et al.*,[10] demonstrated that, using physically constrained GO membranes, the rejection properties of a membrane can be measured using forward osmosis, where the draw side of the membrane contains 3 M sucrose and the feed contains 0.1 M NaCl. Using this technique they were able to achieve salt rejection of ~97% and a water flux of 0.5 L m^{-2} h^{-1}.[10] By replicating this technique here using the MoS_2/SY membrane (5 μm thick), we achieved an improved rejection of ~99% while also recording a water flux five times higher than that of a GO membrane of similar thickness (2.5 L m^{-2} h^{-1}). Table S2 compares the performance of various GO-based membranes reported in the literature as well as the functionalized MoS_2 membranes. This significant increase in water permeability, while also increasing the NaCl rejection, demonstrates the improved performance these functionalized MoS_2 membranes have over similar technologies.

The water permeability, calculated using external pressure, is also summarized for each corresponding membrane in Figure 4a, where notably the CV functionalization actually leads to an increase in the water flux compared to the pristine MoS_2 membrane, demonstrating improved water transport properties while maintaining excellent ionic rejection. Our use of dye functionalization provides an effective yet simple route to tune the permeability performance of these membranes. In comparison, unfunctionalized membranes have been recently reported to have high $MgCl_2$ permeability, which was attributed to the almost equal charge density ratio between the cation and anions.[18] The predominant transport mechanism in this previous work was attributed to an electrostatic attraction between the cations in solution and the negatively charged MoS_2 channels, with atomic radii only affecting the transport above the critical channel width. In contrast, the dye-functionalization approach reported here provides an unexpected route to tune the permeability performance of these membranes. This change in permeability after functionalization can be attributed to a change in the surface charge near the membrane interface. By attaching the charged dye molecules to the surface of the MoS_2, we can alter the double-layer formation when exposed to ionic solutions and thus tune the permeability of the functionalized membrane.

The filtration performance of each of the commonly found ionic solutes in seawater was analyzed. The rejection rates, calculated after 3 h with a 1000× concentration gradient for

DOI: 10.1021/acsnano.7b05124
ACS Nano 2017, 11, 11082–11090

each of KCl, NaCl, Na_2SO_4, $CaCl_2$, and $MgCl_2$, are shown in Figure 4b as a function of hydrated cationic radius (listed in Table S3). The rejection rates for the MoS_2/SY membrane show a consistent ~98% rejection for each of the analyzed solutes, increasing to almost 100% for Mg^{2+}, while the MoS_2/CV shows a slightly larger variation with rejection rates between 92 and 100%. The permeation rate of these ionic solutes can be calculated by measuring the concentration determined from ICP-OES as a function of time (Figure 4c). Joshi *et al.* reported an ion permeation rate of ~2 mol m^{-2} h^{-1} using GO membranes of a similar thickness (5 μm) and an identical feed concentration (1 M).[7] Here we show that ionic permeation rates an order of magnitude lower than this can be achieved using the dye-functionalized MoS_2 membranes. Permeation rates of ~0.15 mol m^{-2} h^{-1} were measured for the K^+, Na^+, and Ca^{2+}, and a further order of magnitude improvement was measured for the Mg^{2+} at ~0.025 mol m^{-2} h^{-1}. This, combined with the significantly increased water permeation rate, indicates that these membranes have great promise as the material of choice for desalination and filtration applications. The mechanism responsible for the ionic sieving effect is a combination of size-based exclusion, evident from the relationship between the rejection rates and hydrated ionic radius, but also related to the charge of the ions as the dye functionalization alters the MoS_2 surface chemistry with minimal effect on its interlayer spacing.

Permeation of Mixed Ionic Solutes. To better replicate real world rejection properties of these membranes, a mixed ionic solution of synthetic seawater (SSW) was tested, shown schematically in Figure 5 inset. The concentration of the ionic solutes was certified as matching the standard composition of seawater, with the highest concentration components being NaCl (0.420 M), $MgCl_2{\cdot}6H_2O$ (0.0556 M), Na_2SO_4 (0.0288 M), $CaCl_2.2H_2O$ (0.0105 M), and KCl (0.00926 M). Figure 5 plots the rejection rate for each of the cationic components of the SSW after 3 h as a function of the hydrated radii. Unlike the single ionic component solutions, the larger radius divalent ions (Ca^{2+} and Mg^{2+}) appear to have a poorer rejection rate than the smaller monovalent ions. Although both MoS_2/CV and MoS_2/SY membranes still show good rejection rates of >80%, this difference can be attributed to their higher charge density leading to a stronger electrostatic interaction with the abundant Cl^- anions present in the mixed solute. The permeation properties of SSW for differing thickness membranes are shown in Figure S12.The interaction between multiple ionic components has not been analyzed previously for similar laminar membranes and remains an area that must be better understood to realize industrial applications.

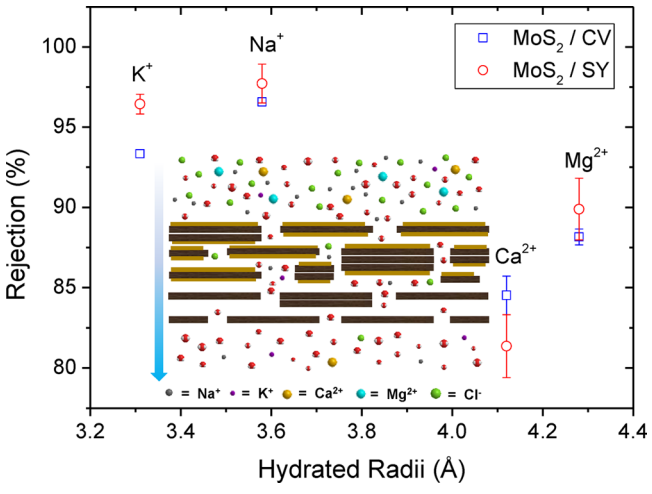

Figure 5. Rejection properties for MoS_2/CV and MoS_2/SY membranes (6 μm thick) for synthetic seawater containing mixed ionic solutes. Inset shows a schematic of the filtration of the mixture of solvated ions found in synthetic seawater.

Characterization of Functionalized MoS_2 Membranes. To better understand the chemical functionalization process, which is key to filtration, Raman and X-ray photoelectron spectroscopies were utilized to analyze the pristine and dye treated MoS_2 membranes. The various characterization techniques were performed on membranes which had been used for multiple filtration experiments and immersed in solution for several months before analysis. Figure 6a compares the Raman spectra of the pristine MoS_2 membrane, with the characteristic E_{2g} and A_{1g} MoS_2 peaks labeled, the raw dye (CV) powder, and the functionalized MoS_2 membrane (MoS_2/CV). The characteristic peaks for the CV are clearly present on the functionalized membrane, although shifted by ~2 cm^{-1} due to doping. The Raman analysis for the other dye-functionalized membranes is shown in Figure S13. This Raman analysis was performed after the functionalized membrane has undergone multiple cleaning treatments with water and has been submerged in multiple aqueous solutions for prolonged periods of time (>6 months), indicating that the dye functionalization is robust and occurs *via* chemisorption, rather than a weaker physisorption mode. This is supported by the XPS analysis shown in Figure 6b–c where a dramatic difference in the Mo_{3d} peak is seen after functionalization. The change in the spectrum corresponds to a significant increase in the amount of octahedral (Mo^{6+}) coordinated molybdenum atoms and indicates that the CV molecules have become attached to the molybdenum within the membrane. Successful functionalization is also confirmed by shifts in binding energy due to charge transfer in the sulfur peaks as well as the presence of bonded nitrogen atoms from the structure of CV itself. Further XPS analysis is presented in Figures S14–S15.

The difference in surface chemistry and roughness is also reflected in the measured water contact angle of the membrane, which approaches super hydrophobicity for the MoS_2/CV surface. In order to understand the wettability of the MoS_2 membranes before and after dye functionalization, water contact angle (WCA) and salt solution contact angle (SCA) were measured by placing ultrapure water and 1 M NaCl droplets on the surface of the MoS_2 membrane ($\theta_{liquid|MoS_2\ membranes}$) (see Figures S16–S17). The WCA for pristine MoS_2 membranes is ~106°, which is higher than was found in previous works (~97°), and is dominated by the sulfur surface termination resulting in the hydrophobic wetting properties of MoS_2.[25,26] The difference in WCA values can be attributed to differences in material preparation and surface roughness during membrane filtration. Interestingly, the surface of the MoS_2/CV membrane displays a WCA of over 140°, approaching superhydrophobicity (>150°). This phenomenon can be explained by the chemical functionalization that changes the MoS_2 surface chemistry, combined with the high surface roughness. This corresponds to the change in surface roughness after CV and SY functionalization, as seen in the SEM images shown in Figure S18. A similar effect has been reported by Choi

DOI: 10.1021/acsnano.7b05124
ACS Nano 2017, 11, 11082–11090

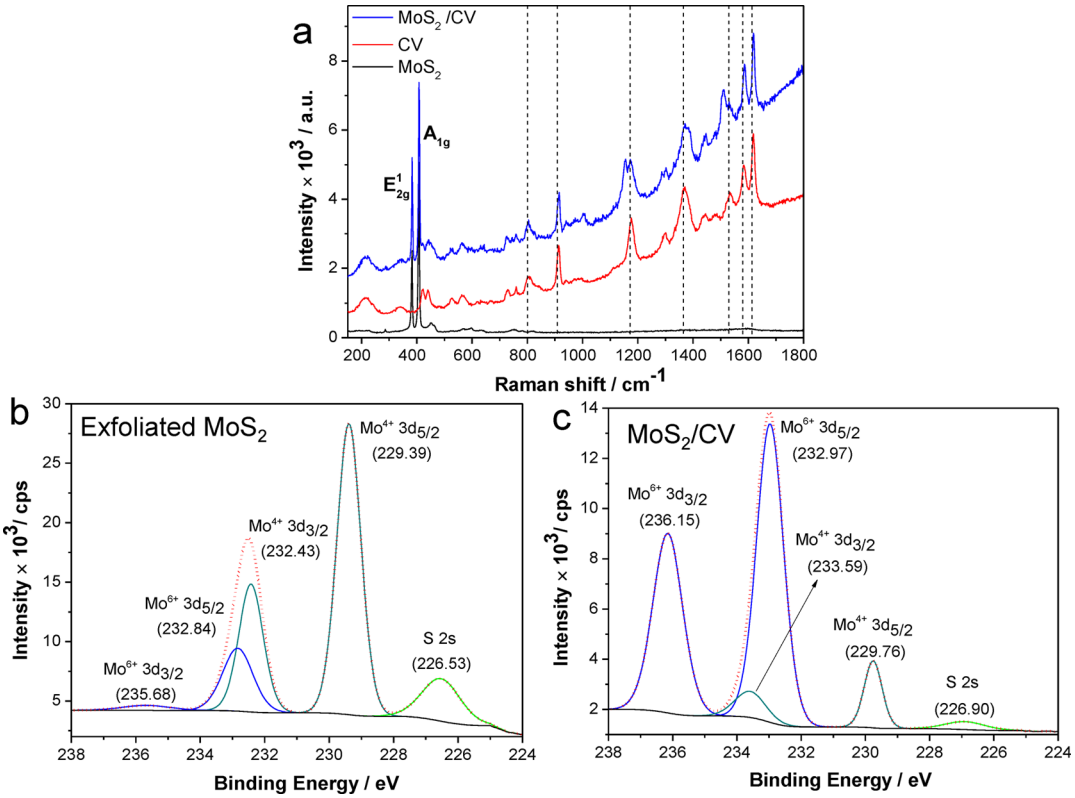

Figure 6. (a) Raman spectra from the pristine MoS_2 membrane, crystal violet (CV) powder, and a CV-functionalized MoS_2 membrane (MoS_2/CV). XPS spectra of the Mo_{3d} region for a pristine exfoliated MoS_2 membrane (b) and a CV-functionalized membrane (c).

et al.,[27] who measured a WCA of almost 160° for crumpled MoS_2 nanoflowers with high surface roughness. Based on these WCA measurements, the high water permeation rates of the MoS_2/CV membranes can be attributed to the near superhydrophobic surface properties which result in minimal interaction between the water molecules and the functionalized MoS_2 nanochannels.

CONCLUSIONS

In conclusion, we report a simple, low-cost route to produce membranes capable of removing common salts, including NaCl, from water at room temperature. The method, based on nontoxic organic-functionalized MoS_2 laminar membranes, is capable of reducing NaCl concentration from levels found in seawater to concentrations suitable for drinking or plant irrigation with a single pass of a membrane a few microns thick. The water fluxes of these membranes are substantially higher than those of GO membranes of comparable thickness, and the trivial energy requirements of this method compared to existing approaches to water purification, such as reverse osmosis and distillation, mean the method is potentially transformative for the many areas of the world currently defined as "water-stressed". The approach is easily tunable *via* variation of the organic modifier functionalization molecule as well as applicable to other 2D materials and their respective chemistries, and this means the approach can be optimized for a variety of technologically important separations.

METHODS

MoS_2 Membrane Fabrication. MoS_2 dispersions were produced by exfoliating commercially available MoS_2 powder through the well-established process of ultrasonication in solvent.[28,29] To reduce solvent contamination and decrease the toxicity of the process here, MoS_2 powder was exfoliated in a mixture of isopropanol (IPA) and water (1:1 v/v) at a concentration of 10 mg/mL *via* bath ultrasonication for 12 h. This solvent ratio has previously been demonstrated to produce high yields of exfoliated MoS_2 flakes, with minimal surface contamination.[30,31] After ultrasonication, the dispersions were centrifuged twice at 6000 rpm (3139 g) for 30 min to remove any unexfoliated material and to ensure a narrow distribution of flake dimensions and thicknesses. This solvent-stabilized dispersion of exfoliated MoS_2 flakes was then filtered and collected on a PVDF membrane (0.1 μm pores) to a specific thickness (1 to 12 μm), as indicated, to produce the MoS_2 laminate membrane. The PVDF supported MoS_2 membrane can be folded without any visible damage of the MoS_2 flakes. For testing, the membrane was then supported on both sides with polyethylene terephthalate (PET) and epoxy glue with a defined area.

Dye Functionalization of the MoS_2 Membranes. Crystal violet (CV), sunset yellow (SY), and neutral red (NR) were each used as cationic (at pH 7), anionic (pH 7), and neutral (pH 9) dyes, respectively, to functionalize the MoS_2 membranes. 50.0 mL of 0.1 mM aqueous solutions of the dyes were prepared as a feed side and 50.0 mL of ultrapure water as the permeate side. The pH of the NR solution was altered using 1 M NaOH to obtain the neutral form of NR molecules.[32] The concentration of dyes in both feed and permeate sides was determined by UV−vis spectrophotometry over 21 days. After dye functionalization, each membrane was cleaned using ultrapure water under hydrostatic pressure for over a week to remove any residual dye molecules inside the membranes. This cleaning process was repeated twice until no unbound dye molecules could be detected. This was verified using electrospray ionization mass spectrometry.

Electron Microscopy. An FEI Titan 80−200 ChemiSTEM equipped with probe-side aberration correction and an X-FEG electron source was used for the aberration-corrected scanning transmission electron microscope (STEM) imaging and EELS analysis. STEM experiments were performed using an acceleration voltage of

DOI: 10.1021/acsnano.7b05124
ACS Nano 2017, 11, 11082−11090

200 kV, a convergence angle of 21 mrad, and beam currents of 90 pA and 400 pA for imaging and EELS acquisition, respectively.

EELS data was acquired using a GIF Quantum ER spectrometer, with an energy dispersion of 0.25 eV and a collection angle of 38 or 62 mrad. In standard STEM imaging mode, the collection angles of the annular detectors were 23−41 mrad and 48−190 mrad, for low-angle annular dark field and high-angle annular dark field, respectively. EELS spectrum images have been denoised by principal component analysis (Poissonian noise normalized) as implemented in the HyperSpy python library.[33] The principal component analysis scree plot and the loadings of the principal components were carefully analyzed to determine which components can be associated with signals and therefore considered for the reconstruction. The number of components used in the reconstruction ranged between 6 and 10. The EELS elemental maps have been obtained from the spectrum image by measuring the integrated intensity in the corresponding edge (Mo-$M_{2,3}$ at 392 eV and S-$L_{2,3}$ at 165 eV). The background has been subtracted by fitting a power law function in the region preceding the edge.[34] The cross-sectional TEM specimens have been prepared by the wedge mechanical polishing technique followed by low-energy (0.2−1 keV) Xe^+ ion polishing.

SEM images were obtained using an FEI XL30 FEG ESEM. Images were obtained with an accelerating voltage of 15 kV, under high-vacuum conditions utilizing secondary electron detection.

Raman Spectroscopy. MoS_2 membranes, before and after dye functionalization, were analyzed by Raman spectroscopy. Confocal Raman spectroscopy was conducted using a Renishaw inVia microscope with a 532 nm (2.33 eV) excitation with a power of ∼1 mW, a 50× objective (1 μm of laser spot diameter), and a grating of 1800 l/mm to achieve a spectral resolution of ∼1 cm^{-1}.

X-ray Photoelectron Spectroscopy. X-ray photoelectron spectroscopy (XPS) analysis was performed with a Kratos Axis Ultra spectrometer, with excitation from a focused monochromated Al Kα source (1486.6 eV) and using an electron flood gun for charge neutralization. All XPS spectra were calibrated using adventitious carbon (C 1s) at 284.8 eV, and the atomic percentage of the peaks were determined by optimized peak fit using a nonlinear Shirley-type background (70% Gaussian and 30% Lorentzian line shapes).

Powder X-ray Diffraction. Powder X-ray diffraction (PXRD) patterns of the MoS_2, bulk and after exfoliation, to form membranes as well as after dye functionalization, were obtained using a PANalytical X'Pert X-ray diffractometer. Using a Cu−Kα radiation source operating at 40 kV and 30 mA, the patterns were recorded while spinning in the range 2θ = 5−45°, with a step size of 0.017° and a scan step time of 66 s. The position of the (002) peak was used to calculate d-spacing of the materials according to Bragg's law. All X-ray patterns were corrected using the PVDF peak at 2θ = 20.17° as a reference peak.

Determination of Water Permeation Rate. Water permeation rates were determined using two different techniques. First, the osmotic pressure technique depending on concentration of solute was calculated using van't Hoff's law:[35] $\Pi = i[C_{sucrose}]RT$, where Π is osmotic pressure, i is the van't Hoff factor (assumed to be 1 for sucrose), $[C_{sucrose}]$ is the concentration of sucrose solution (1 M), R is the gas constant, and T is the absolute temperature; this corresponds to an osmotic pressure of ∼25 bar at room temperature. A 1 M sucrose solution and distilled water are placed into an H cell at the same liquid levels with the MoS_2 sandwich membranes inserted.

Second, external pressure was also used to determine the water permeation rate using a dead-end filtration setup with a constant pressure at 1.0 bar. The MoS_2 sandwich membrane was inserted and sealed in a syringe holder with two O-rings at the top and bottom to protect against leakage. The water permeation rate was calculated by weighing the volume of water passing through the membrane under constant pressure as a function of time.

Ionic Permeation Experiments. Ionic permeation was carried out using a bespoke H-beaker setup as shown in Figure 3a. Resistivity and potentiometric measurements were performed simultaneously to measure the decreasing resistivity of the permeate side and the potential difference between two Ag/AgCl reference electrodes in both feed and permeate sides under zero current conditions. Both the feed and permeate sides underwent constant stirring to minimize the concentration gradient over 3 h. The starting concentrations in the feed and permeate sides are 1 M and 1 mM, respectively, with equal volumes of solute (50.0 cm^3). *In situ* measurements of the change in ionic concentration as well as *ex situ* measurements of the ion concentration were determined by inductively coupled plasma optical emission spectrometry (ICP-OES) after 3 h. Salt rejection (%) was calculated as $1 - C_{MoS_2}/C_{PVDF}$, where C_{MoS_2} and C_{PVDF} are the increased ions concentration in the presence and absence the MoS_2 lamellar membranes, respectively, in the permeate side.

ASSOCIATED CONTENT

Supporting Information

The Supporting Information is available free of charge on the ACS Publications website at DOI: 10.1021/acsnano.7b05124.

Further membrane characterization including XRD, Raman, XPS, TEM, ζ potentials, contact angle experiments, and further ion permeation results and analysis (PDF)

AUTHOR INFORMATION

Corresponding Authors

*E-mail: Robert.Dryfe@manchester.ac.uk.
*E-mail: Mark.Bissett@manchester.ac.uk.

ORCID

Stephen D. Worrall: 0000-0003-1969-3671
Sarah J. Haigh: 0000-0001-5509-6706
Robert A. W. Dryfe: 0000-0002-9335-4451
Mark A. Bissett: 0000-0002-8908-7960

Present Address

[‖]School of Earth and Environmental Science, University of Manchester, Oxford Road, Manchester, UK, M13 9PL.

Author Contributions

M.A.B. conceived and designed the project with R.A.W.D. and wrote the manuscript with contributions from all authors. W.H. prepared the samples, performed the measurements, and carried out data analysis. E.P. performed the STEM characterization and sample preparation with contributions from S.J.H. S.D.W. performed XRD characterization and data analysis. All authors contributed to interpretation and discussion of the results.

Notes

The authors declare the following competing financial interest(s): This work is the subject of a patent application (PCT/GB2017/050957).

ACKNOWLEDGMENTS

W.H. wishes to acknowledge the Development and Promotion of Science and Technology Talents Project (DPST), Royal Government of Thailand scholarship. S.J.H. acknowledges funding from the Defence Threat Reduction Agency (HDTRA1-12-1-0013) and Engineering and Physical Sciences Research Council, UK (EP/K016946/1, EP/L01548X/1, EP/M010619/1 and EP/P009050/1). R.A.W.D. wishes to acknowledge the EPSRC (EP/K016954/1). All research data supporting this publication are directly available within this publication and the corresponding Supporting Information as well as available from the corresponding authors upon reasonable request.

DOI: 10.1021/acsnano.7b05124
ACS Nano 2017, 11, 11082−11090

REFERENCES

(1) Shannon, M. A.; Bohn, P. W.; Elimelech, M.; Georgiadis, J. G.; Marinas, B. J.; Mayes, A. M. Science and Technology for Water Purification in the Coming Decades. *Nature* **2008**, *452*, 301−310.

(2) Pendergast, M. M.; Hoek, E. M. V. A Review of Water Treatment Membrane Nanotechnologies. *Energy Environ. Sci.* **2011**, *4*, 1946−1971.

(3) Cheng, C.; Jiang, G.; Garvey, C. J.; Wang, Y.; Simon, G. P.; Liu, J. Z.; Li, D. Ion Transport in Complex Layered Graphene-Based Membranes With Tuneable Interlayer Spacing. *Sci. Adv.* **2016**, *2*, e1501272.

(4) Huang, L.; Zhang, M.; Li, C.; Shi, G. Graphene-Based Membranes for Molecular Separation. *J. Phys. Chem. Lett.* **2015**, *6*, 2806−2815.

(5) Sun, P.; Wang, K.; Zhu, H. Recent Developments in Graphene-Based Membranes: Structure, Mass-Transport Mechanism and Potential Applications. *Adv. Mater.* **2016**, *28*, 2287−2310.

(6) Celebi, K.; Buchheim, J.; Wyss, R. M.; Droudian, A.; Gasser, P.; Shorubalko, I.; Kye, J.-I.; Lee, C.; Park, H. G. Ultimate Permeation Across Atomically Thin Porous Graphene. *Science* **2014**, *344*, 289−292.

(7) Joshi, R. K.; Carbone, P.; Wang, F. C.; Kravets, V. G.; Su, Y.; Grigorieva, I. V.; Wu, H. A.; Geim, A. K.; Nair, R. R. Precise and Ultrafast Molecular Sieving Through Graphene Oxide Membranes. *Science* **2014**, *343*, 752−754.

(8) Sun, P.; Zhu, M.; Wang, K.; Zhong, M.; Wei, J.; Wu, D.; Xu, Z.; Zhu, H. Selective Ion Penetration of Graphene Oxide Membranes. *ACS Nano* **2013**, *7*, 428−437.

(9) Yeh, C.-N.; Raidongia, K.; Shao, J.; Yang, Q.-H.; Huang, J. On the Origin of the Stability of Graphene Oxide Membranes in Water. *Nat. Chem.* **2015**, *7*, 166−170.

(10) Abraham, J.; Vasu, K. S.; Williams, C. D.; Gopinadhan, K.; Su, Y.; Cherian, C. T.; Dix, J.; Prestat, E.; Haigh, S. J.; Grigorieva, I. V.; Carbone, P.; Geim, A. K.; Nair, R. R. Tunable Sieving of Ions Using Graphene Oxide Membranes. *Nat. Nanotechnol.* **2017**, *12*, 546−550.

(11) Han, Y.; Xu, Z.; Gao, C. Ultrathin Graphene Nanofiltration Membrane for Water Purification. *Adv. Funct. Mater.* **2013**, *23*, 3693−3700.

(12) Hu, M.; Mi, B. Enabling Graphene Oxide Nanosheets as Water Separation Membranes. *Environ. Sci. Technol.* **2013**, *47*, 3715−3723.

(13) Dervin, S.; Dionysiou, D. D.; Pillai, S. C. 2D Nanostructures for Water Purification: Graphene and Beyond. *Nanoscale* **2016**, *8*, 15115−15131.

(14) Liu, G.; Jin, W.; Xu, N. Two-Dimensional-Material Membranes: A New Family of High-Performance Separation Membranes. *Angew. Chem., Int. Ed.* **2016**, *55*, 13384−13397.

(15) Ren, C. E.; Hatzell, K. B.; Alhabeb, M.; Ling, Z.; Mahmoud, K. A.; Gogotsi, Y. Charge- and Size-Selective Ion Sieving Through $Ti_3C_2T_x$ MXene Membranes. *J. Phys. Chem. Lett.* **2015**, *6*, 4026−4031.

(16) Sun, L.; Ying, Y.; Huang, H.; Song, Z.; Mao, Y.; Xu, Z.; Peng, X. Ultrafast Molecule Separation Through Layered WS_2 Nanosheet Membranes. *ACS Nano* **2014**, *8*, 6304−6311.

(17) Sun, L.; Huang, H.; Peng, X. Laminar MoS_2 Membranes for Molecule Separation. *Chem. Commun.* **2013**, *49*, 10718−10720.

(18) Deng, M.; Kwac, K.; Li, M.; Jung, Y.; Park, H. G. Stability, Molecular Sieving, and Ion Diffusion Selectivity of a Lamellar Membrane from Two-Dimensional Molybdenum Disulfide. *Nano Lett.* **2017**, *17*, 2342−2348.

(19) Heiranian, M.; Farimani, A. B.; Aluru, N. R. Water Desalination With A Single-Layer MoS_2 Nanopore. *Nat. Commun.* **2015**, *6*, 8616.

(20) Liu, R.; Arabale, G.; Kim, J.; Sun, K.; Lee, Y.; Ryu, C.; Lee, C. Graphene Oxide Membrane for Liquid Phase Organic Molecular Separation. *Carbon* **2014**, *77*, 933−938.

(21) Huang, K.; Liu, G.; Lou, Y.; Dong, Z.; Shen, J.; Jin, W. A Graphene Oxide Membrane with Highly Selective Molecular Separation of Aqueous Organic Solution. *Angew. Chem., Int. Ed.* **2014**, *53*, 6929−6932.

(22) Talyzin, A. V.; Hausmaninger, T.; You, S.; Szabo, T. The Structure of Graphene Oxide Membranes in Liquid Water, Ethanol and Water-Ethanol Mixtures. *Nanoscale* **2014**, *6*, 272−281.

(23) Kim, J.; Kwon, S.; Cho, D.-H.; Kang, B.; Kwon, H.; Kim, Y.; Park, S. O.; Jung, G. Y.; Shin, E.; Kim, W.-G.; Lee, H.; Ryu, G. H.; Choi, M.; Kim, T. H.; Oh, J.; Park, S.; Kwak, S. K.; Yoon, S. W.; Byun, D.; Lee, Z.; et al. Direct Exfoliation and Dispersion of Two-Dimensional Materials in Pure Water *Via* Temperature Control. *Nat. Commun.* **2015**, *6*, 8294.

(24) Feng, J.; Graf, M.; Liu, K.; Ovchinnikov, D.; Dumcenco, D.; Heiranian, M.; Nandigana, V.; Aluru, N. R.; Kis, A.; Radenovic, A. Single-Layer MoS_2 Nanopores as Nanopower Generators. *Nature* **2016**, *536*, 197−200.

(25) Tao, L.; Duan, X.; Wang, C.; Duan, X.; Wang, S. Plasma-Engineered MoS_2 Thin-Film as an Efficient Electrocatalyst for Hydrogen Evolution Reaction. *Chem. Commun.* **2015**, *51*, 7470−7473.

(26) Heyne, M. H.; Chiappe, D.; Meersschaut, J.; Nuytten, T.; Conard, T.; Bender, H.; Huyghebaert, C.; Radu, I. P.; Caymax, M.; de Marneffe, J. F.; Neyts, E. C.; De Gendt, S. Multilayer MoS_2 Growth by Metal and Metal Oxide Sulfurization. *J. Mater. Chem. C* **2016**, *4*, 1295−1304.

(27) Choi, J.; Mun, J.; Wang, M. C.; Ashraf, A.; Kang, S. W.; Nam, S. Hierarchical, Dual-Scale Structures of Atomically Thin MoS_2 for Tunable Wetting. *Nano Lett.* **2017**, *17*, 1756−1761.

(28) Nicolosi, V.; Chhowalla, M.; Kanatzidis, M. G.; Strano, M. S.; Coleman, J. N. Liquid Exfoliation of Layered Materials. *Science* **2013**, *340*, 1226419.

(29) Coleman, J. N.; Lotya, M.; O'Neill, A.; Bergin, S. D.; King, P. J.; Khan, U.; Young, K.; Gaucher, A.; De, S.; Smith, R. J.; Shvets, I. V.; Arora, S. K.; Stanton, G.; Kim, H.-Y.; Lee, K.; Kim, G. T.; Duesberg, G. S.; Hallam, T.; Boland, J. J.; Wang, J. J.; et al. Two-Dimensional Nanosheets Produced by Liquid Exfoliation of Layered Materials. *Science* **2011**, *331*, 568−571.

(30) Shen, J.; He, Y.; Wu, J.; Gao, C.; Keyshar, K.; Zhang, X.; Yang, Y.; Ye, M.; Vajtai, R.; Lou, J.; Ajayan, P. M. Liquid Phase Exfoliation of Two-Dimensional Materials by Directly Probing and Matching Surface Tension Components. *Nano Lett.* **2015**, *15*, 5449−5454.

(31) Shen, J.; Wu, J.; Wang, M.; Dong, P.; Xu, J.; Li, X.; Zhang, X.; Yuan, J.; Wang, X.; Ye, M.; Vajtai, R.; Lou, J.; Ajayan, P. M. Surface Tension Components Based Selection of Cosolvents for Efficient Liquid Phase Exfoliation of 2D Materials. *Small* **2016**, *12*, 2741−2749.

(32) Moulik, S. P.; Paul, B. K.; Mukherjee, D. C. Acid-Base Behavior of Neutral Red in Compartmentalized Liquids (Micelles and Microemulsions). *J. Colloid Interface Sci.* **1993**, *161*, 72−82.

(33) Peña, F. d. l.; Ostasevicius, T.; Fauske, V. T.; Burdet, P.; Jokubauskas, P.; Nord, M.; Sarahan, M.; Johnstone, D. N.; Prestat, E.; Taillon, J.; Caron, J.; Furnival, T.; MacArthur, K. E.; Eljarrat, A.; Mazzucco, S.; Migunov, V.; Aarholt, T.; Walls, M.; Winkler, F.; Martineau, B., et al. *hyperspy/hyperspy*, v1.2, 2017, 10.5281/zenodo.345099 (Accessed March 2, 2017).

(34) Egerton, R. F. *Electron Energy-Loss Spectroscopy in the Electron Microscope*. 3rd ed.; Springer: New York, 2011; Vol *10*.

(35) Atkins, P.; Paula, J. d. *Physical Chemistry*. 7th ed.; Oxford University Press: Oxford, UK, 2002.

DOI: 10.1021/acsnano.7b05124
ACS Nano 2017, 11, 11082−11090